DFT and experimental study of elemental mercury (Hg^0) removal by 2D-g-C$_3$N$_4$

Liu, Guoshuai; Yan, Qun; Zhou, Yanan; Zhang, Xuedong; Spanjers, Henri

DFT and experimental study of elemental mercury (Hg⁰) removal by 2D-g-C₃N₄

Guoshuai Liu [a,c], Qun Yan [a,*], Yanan Zhou [b,*], Xuedong Zhang [c], Henri Spanjers [c]

[a] School of Environmental and Civil Engineering, Jiangnan University, Wuxi 214122, China
[b] School of Chemical Engineering, Sichuan University, Chengdu, Sichuan 610065, China
[c] Sanitary Engineering, Water Management, Delft University of Technology, Stevinweg 1, 2628 CN Delft, the Netherlands

ARTICLE INFO

ABSTRACT

2D-g-C₃N₄ nanosheet was prepared and employed for the adsorption of elemental mercury (Hg⁰). The g-C₃N₄ was analyzed through X-ray diffraction (XRD), scanning electron microscope (SEM) and Fourier transform infrared spectroscopy (FT-IR) methods, and the results showed that the prepared sample was well-defined 2D-nanosheet. The 2D-g-C₃N₄ sorbent exhibited a high Hg⁰ removal efficiency (> 90%) at the condition of temperature 120 °C. To investigate the mechanism of Hg⁰ adsorption on the 2D-g-C₃N₄ surface, corresponding theoretical exploration based on the first principle prediction and X-ray photoelectron spectroscopy (XPS) test was implemented. The DFT calculation results showed that Hg⁰ was strongly bound to the B_1 site of the g-C₃N₄ surface with an adsorption energy change of -162.2 kJ mol⁻¹, the equilibrium distance of Hg-C was 3.473 Å, and electron transfer between Hg and C atoms was 0.02. The results of XPS showed the main species of mercury was HgO on the surface of 2D-g-C₃N₄ sample and the interaction between C₃N₄ surface and Hg⁰ was physisorption. This study provides a demonstration of proof-of-concept demonstration that g-C₃N₄ is a promising sorbent capable of capturing Hg⁰, and presents in-depth understanding of Hg⁰ adsorption mechanism on 2D-g-C₃N₄ sorbent.

1. Introduction

As a highly toxic heavy metal, elemental mercury (Hg⁰) pollution is a very serious issue concerning both environments and social security, and the research on mercury pollution control has been widely concerned and focused [1], [2]. In order to effectively eliminate the Hg⁰ pollution, the Minamata Convention on Mercury has developed an international convention to limit mercury emissions [3], [4]. As the largest coal-consuming country in the world, it is estimated that China emitted about 25−40% of global mercury annually [3]. In this regards, China's government also developed the latest Emission Standard of Air Pollutants for Thermal Power Plants (GB13223–2011), which aims to reduce the mercury emissions from power plants.

The removal of Hg⁰ has been intensively studied because Hg⁰ presents high thermodynamic stability, strong volatility, and high toxicity, and is also slightly soluble in water and prone to be bio-accumulated [5], [6]. As being widely known, the main anthropogenic source of mercury pollution is the combustion of fossil fuels [7]. In this context, the development of effective approaches in mercury removal is of great practical and scientific significance. Amongst the various chemical or physical methods of Hg⁰ removal, adsorption technology is regarded as one of the most promising removal methods because of its high efficiency,

simplicity and operability [8,9]–[10]. A large number of researchers focus on developing new materials or new adsorbents for the adsorption of mercury. For example, activated carbon (AC) [11], Fe₂O₃ [12], fly ash [9], MnOₓ [13], TiO₂ and Co₃O₄ [14],[15]. Although a large of quantities of studies on mercury adsorption have been carried out, the mechanism of surface adsorption of mercury and adsorbents has been often overlooked.

Amongst the various adsorbents, emerging two-dimensional (2D) materials have demonstrated their privileges toward target adsorption due to their surface characteristics such as high surface energy, large surface area and multiple active sites [16], [17]. Thus, the development of 2D adsorbents is highly appreciated and intriguing for effective and efficient adsorption [18,19]–[20]. As an emerging 2D metal-free material, graphitic carbon nitride (g-C₃N₄) has drawn substantial attention because of its relative high availability, and particularly its structural stability and unique surface properties [21,22]–[23]. The framework topology of g-C₃N₄ is defect-rich and N-bridged "poly (triazine)", and it presents good physical and chemical stability, even under extreme acidic conditions or/and high temperature [24], [25]. More importantly, g-C₃N₄ is an environmentally friendly material, which presents no potential threat of direct and secondary pollution to organisms and the environment [26–28]–[29]. Besides, the in-built functional groups of

g-C$_3$N$_4$ are well-characterized ligands -NH$_2$/-NH-/=N-, and it is proven that these surface sites can function as the basic active sites to selectively adsorb metal atoms and organic compounds through complexation surface interaction [30]. Regarding to the Hg^0 removal by g-C$_3$N$_4$ material, Liu et al. carried out a study on g-C$_3$N$_4$ based sorbents for Hg^0 removal, and their results showed the g-C$_3$N$_4$ modified by MnO$_2$ presented better performance in Hg^0 adsorption than pristine g-C$_3$N$_4$ material [24], and the NO/Hg° catalytic oxidation mechanism by Pd/g-C$_3$N$_4$ catalyst was investigated [26]. Zhang et al. also observed that Co$_3$O$_4$/g-C$_3$N$_4$ hybrids presented the Hg^0 removal efficiency of ~100% under the temperature at or above 120 °C [25], and the BiOIO$_3$/g-C$_3$N$_4$ heterogeneous catalysis was also implemented in Hg0 removal [27]. However, limited theoretical studies have been carried out on the adsorption of Hg^0 on g-C$_3$N$_4$ surface [31]. Hence, theoretical study on the interaction of Hg^0 with g-C$_3$N$_4$ surface in atomic-scale is impending to have an in-depth understanding of the Hg^0 adsorption mechanism.

In the current manuscript, we employed density functional theory (DFT) and also combined the DFT calculations with experimental study of elemental mercury (Hg^0) removal by 2D-g-C$_3$N$_4$ to further unveil the Hg^0 adsorption mechanism. First, the crystalline structure and morphology of as-prepared g-C$_3$N$_4$ nanosheet adsorbent were analyzed using X-ray diffraction (XRD) and electron microscope. Second, the 2D-g-C$_3$N$_4$ was employed to remove Hg° from a simulated flue gas. Third, the DFT calculation and analyses using X-ray photoelectron spectroscopy (XPS) were carried out to understand the intrinsic Hg^0 adsorption and transformation mechanism on the 2D-g-C$_3$N$_4$ surface. Therefore, besides an in-depth understanding of the adsorption characteristic of Hg^0 towards 2D-g-C$_3$N$_4$ nanosheet, the present study also serves as an experimental and theoretical reference for future application of 2D-g-C$_3$N$_4$-based adsorbents.

2. Materials and methods

2.1. Chemicals

The reagents with analytical grade that were purchased from Sinopharm chemical reagent Beijing were used in this work. The reagents were urea, (CO(NH$_2$)$_2$, CAS 57–13–6), and nitric acid (HNO$_3$, 7697–37–2).

2.2. Preparation of 2D-g-C$_3$N$_4$ nanosheet

The g-C$_3$N$_4$ was prepared by pyrolysis of urea. In a typical synthesis procedure, first, 50 g urea sample was put into a covered alumina crucible, and then transferred to a program-controlled muffle furnace with a heating rate of 5 °C min^{-1} for calcination time of 2 h at a target temperature of 500 °C. Afterwards, leaving the furnace to cool down to the ambient condition, then the collected samples were cleaned repeatedly in nitric acid solution and deionized water (DI-water). Finally, the final sample was preserved in a vacuum drying chamber at 60 °C for further characterization and tests.

2.3. Characterization of 2D-g-C$_3$N$_4$ nanosheet

The powder X-ray diffraction (XRD) of the synthesis 2D-g-C$_3$N$_4$ samples was measured using an X-ray diffractometer (Bruke D8 Adv., Germany, CuKα λ=0.15418 nm). The surface morphology of the material was investigated by an FESEM-4800 field emission scanning electron microscope (SEM, Hitachi, Japan). The structure of surface functional groups was detected by an infrared spectrometer (IR Prestige-21, Shimadzu. Japan).

2.4. Elemental mercury (Hg^0) removal measurements

A lab-scale fixed-bed adsorption setup was assembled to explore the uptake capacity of Hg^0 by the sorbents according to the previous studies

[11],[13],[15]. The test of Hg^0 removal was implemented in a fixed-bed reactor under the condition of the gas flow rate of 500 mL min^{-1} and the temperature range of 80 to 240 °C. In a typical procedure, fifty milligrams of g-C$_3$N$_4$ sorbent was used in the fixed-bed quartz reactor under the following reaction conditions: 50 mg g-C$_3$N$_4$ sorbent, heating rate of the fixed bed of 10 °C/min, 4% O$_2$, 500 μg/m^3 of Hg^0, all balanced in N$_2$ with a total gas flow rate of 500 mL/min. The real-time Hg^0 removal efficiency in this current study is defined as η, which can be calculated by the followed Eq. (1):

$$\eta = \left(1 - C_{out}/C_{in}\right) \times 100\% \tag{1}$$

where C$_{in}$ and C$_{out}$ represents the actual time Hg° concentration in the inlet and outlet tube of the setup, respectively.

2.5. Models and computacing methods

All the calculations in this work were conducted with the DMol^3 package. Taking account of computation time and computation cost, and combining the investigations about Hg0 removal, generalized gradient approximation (GGA) Perdew-Burke-Ernzerhof (PBE) method presents more accurate geometry approximations than GGA-PW91, GGA-BLYP and LDA-PWC, and provides the best overall results [1],[32]. Therefore, GGA-PBE method was employed in the current work. Because the version 4.4 of the basis set of double numerical basis with polarization functions (DNP) is the newly optimized set and delivers slightly improved heat formation [33], thus the double numerical basis with polarization functions (DNP, 4.4) was employed in this work [32–34]–[35]. The convergence criteria were set as the force on the atoms less than 0.01 eV Å^{-1}, the stress on the atoms less than 0.02 GPa, the atomic displacement less than 5 × 10^{-4} Å, and the energy change per atom less than 5 × 10^{-6} eV. For Hg atom, the density functional semi-core pseudopotentials (DSPP) were employed and the self-consistent field convergence criterion was set as an energy change of 10^{-6} Ha. Brillouin Zone integrations were performed using a 6 × 6 × 1 Monkhorst-Pack grid. The adsorption energy was calculated according to the following equation:

$$E_{ads} = E_{Hg+surface} - E_{Hg} - E_{surface} \tag{2}$$

where E$_{ads}$ is the adsorption energy, E$_{Hg+surface}$ is the energy of the total adsorption system, E$_{Hg}$ is the energy of the Hg atom, E$_{surface}$ is the energy of exposed C$_3$N$_4$ surface, and the adsorption energy is calculated in kJ/mol. With this definition, a higher negative value of E$_{ads}$ corresponds to a stronger adsorption, and the corresponding adsorption sites were illustrated in Fig. S1.

3. Results and discussion

3.1. 2D-g-C$_3$N$_4$ characterization

XRD analysis was performed to understand the crystal properties of the prepared 2D-g-C$_3$N$_4$ sample, and the corresponding XRD pattern was depicted in Fig. 1. As illustrated in Fig. 1, the obtained XRD spectrum clearly shows two obvious diffraction peaks at 2θ = 27.4° and 2θ = 13.1°, respectively. For the peak at 27.4°, this is the typical interlayer stacking peak of aromatic which well indexes to the (002) plane with a distance d = 0.32 nm (d-spacing determined by HRTEM picture in Fig. S2). For the relative weak peak at 2θ = 13.1°, which is well indexed to the (100) crystal face of g-C$_3$N$_4$, this is the typical in-plane structural packing of tri-s-triazine units with an interface distance of d = 0.68 nm, and the result is in line with the previous reports [36],[37]. The observed two characteristic diffraction peaks indicate that the prepared sample was well crystallized g-C$_3$N$_4$ and is in line with the previous reports [38],[39]. No obvious unknown diffraction peak was observed, which indicates the g-C$_3$N$_4$ was without any impurity. For pilot-scale preparation of g-C$_3$N$_4$, urea is highly appreciated by the properties such as low cost and high availability. Simultaneously, during heat-treated process,
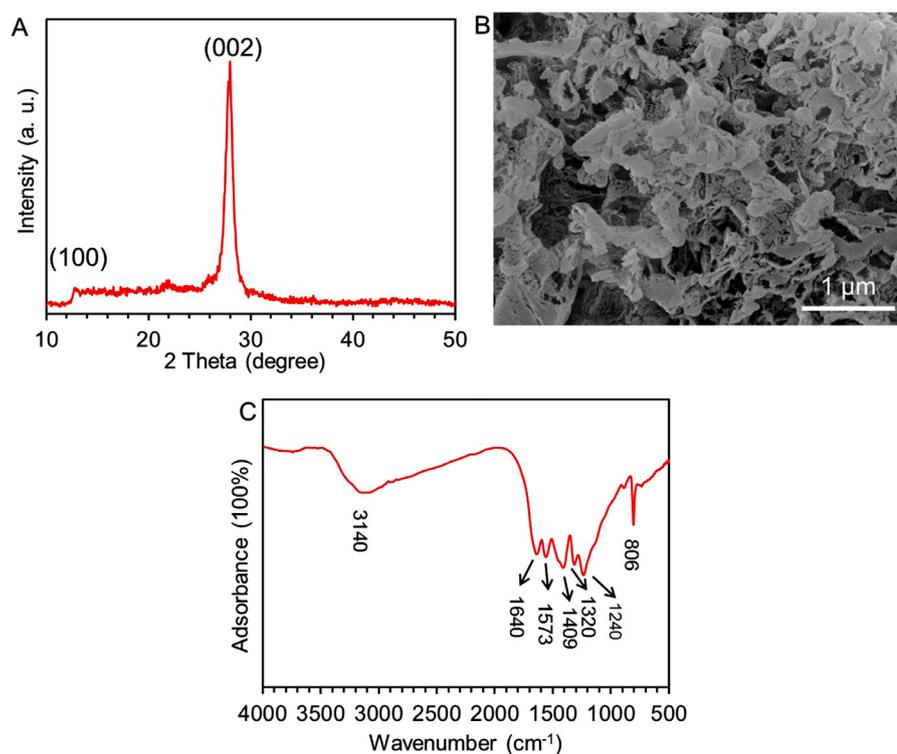
Fig. 1. The XRD pattern (A), SEM (B) and FT-IR (C) curve of as-prepared g-C_3N_4 sample.

self-generating gas bubble would lead to porous structure of g-C_3N_4. As illustrated in Fig. 1B, the collected g-C_3N_4 exhibited the morphology of a typical flat sheet with irregular wrinkles, indicating a typical 2D-g-C_3N_4 sheet surface feature [36]. In order to intensively characterize the surface groups of 2D-g-C_3N_4, the FT-IR spectrum of the sample was investigated and the spectrum is shown in Fig. 1C. As depicted in Fig. 1C, three adsorption bands were observed located at 1409, 1573 and 1640 cm^{-1}, which attributed to the characteristic heptazine-rings vibrations [40]. For the adsorption peak at 1240 and 1320 cm^{-1}, which are the typical amine secondary (2C−N) and tertiary (3C−N) functional group vibrations, respectively [41]. A broad band located at 3140 cm^{-1} is attributed to the −NH_2− and −NH− functional group vibration modes, implying that the monolayer edge or the surface terminated hydrogen atoms were with the existing form of C−NH_2 and 2C−NH in the surface layer structure of 2D-g-C_3N_4 [42]. Besides, the typical bending vibration of heptazine rings for g-C_3N_4 was also identified with a wavenumber of 806 cm^{-1} [41],[43]. Based on the aforementioned results and discussion, it can be concluded that the as-prepared sample was well-defined 2D-g-C_3N_4 sheet. The performance of adsorption removal of Hg° follows.

3.2. The adsorption performance of 2D-g-C_3N_4

The Hg^0 removal performance of prepared 2D-g-C_3N_4 materials was investigated on a laboratory fix-bed reactor [11],[13],[15]. The corresponding Hg^0 removal curve was depicted in Fig. 2A. As shown in Fig. 2A, the adsorption performance of 2D-g-C_3N_4 with the variations in temperature in the range of 80 to 240 °C was investigated, and the corresponding experimental results are shown in Fig. 2B. The 2D-g-C_3N_4 nanosheet exhibited the highest removal efficiency when the temperature was 120 °C, and the Hg^0 removal efficiency of 2D-g-C_3N_4 was decreased when the adsorption temperature was higher than 120 °C. The results might be caused by the sorption mechanism of Hg^0 on 2D-g-C_3N_4 surface, which is physisorption with an exothermic reaction [24],[25], and imply that to reach a high Hg^0 adsorption efficiency operational temperatures higher than 120 °C are not a necessity and also not favored. Furthermore, under the condition of a temperature of 120 °C (4% O_2), as displayed in Fig. 2B, the Hg^0 removal performance reached
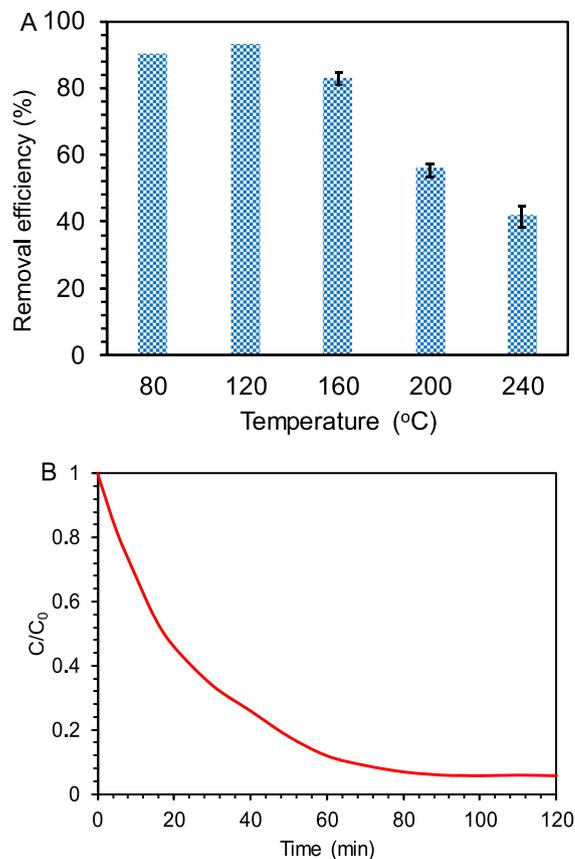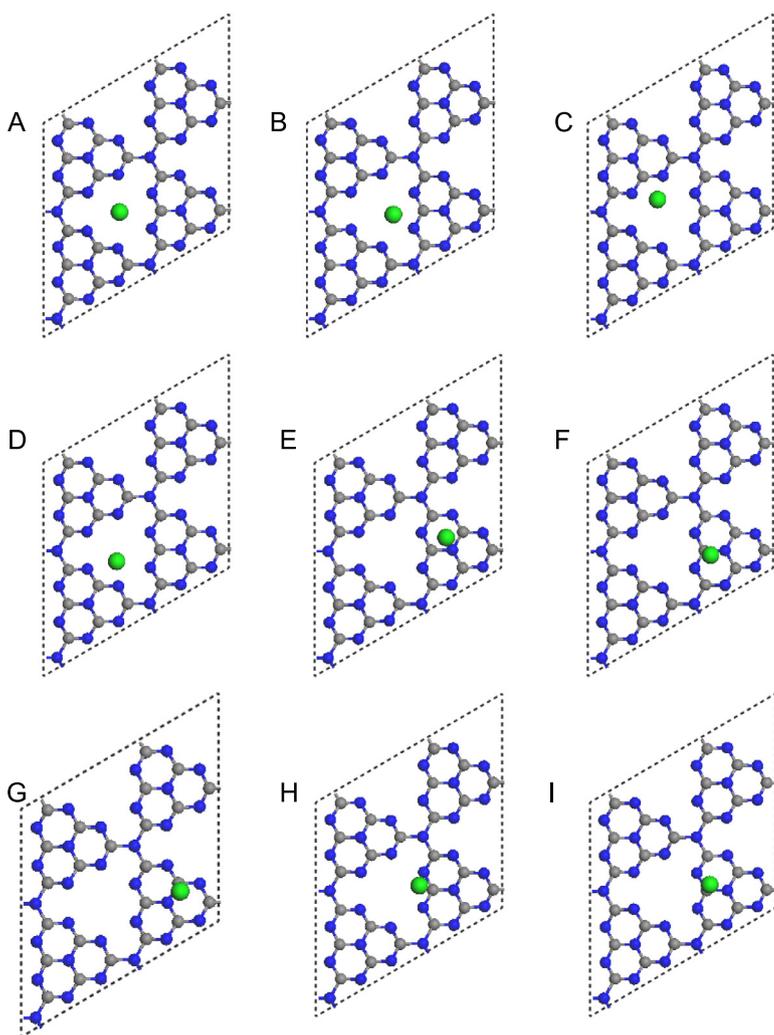

Fig. 2. (A) The Hg^0 removal efficiency of g-C_3N_4 at different temperatures. (B) The performance of g-C_3N_4 nanosheet at 120 °C. The error bars ± SD indicate the measurement in triplicate.

Fig. 3. The optimized structure of Hg^0 adsorption on g-C_3N_4 surface. (A) H_{C1} site; (B) H_{C2} site (C) H_{C3} site; (D) H_{C4} site; (E) H_1 site; (F) H_2 site (G) H_3 site; (H) B_1 site; (I) B_2 site.

the highest 93% removal efficiency with 90 min, which indicates the as-prepared 2D-g-C_3N_4 was able to efficiently adsorb Hg^0.

3.3. DFT research on the Hg^0 adsorption on the g-C_3N_4 surface

The original periodic 2D-g-C_3N_4 surface structure was built and followed a geometry optimization in the points of view of energy and structure stability. To better illustrate the most stable adsorption position, nine possible stable adsorption positions were taken into consideration (Fig. S1) [44], and the corresponding optimized adsorption configurations and results are pictured in Fig. 3. As shown in Fig. 3, the possible sites for Hg adsorption on g-C_3N_4 surface has been taken into consideration denoted as H_C (the Hg atom adsorbs on hollow site) and B (bridge site with Hg atom that adsorbs on the g-C_3N_4 surface). The adsorption energy and the spatial structure parameters for Hg^0-g-C_3N_4 surface are summarized in Table 1. As listed in Table 1, adsorption energy was from −114.8 to −162.2 kJ mol^{-1} in all the configurations of adsorption, and the equilibrium distance ranged from 2.748 Å to 3.498 Å. In the more stable site (B_1), the adsorption energy was −162.2 kJ mol^{-1}. From the adsorption heat viewpoint, the adsorption energy of 162.2 kJ mol^{-1} belongs to the chemisorption according to the fact that the heat of adsorption is in the range of 40–400 kJ mol^{-1} [32]. Whereas, as shown in Fig. S3, the g-C_3N_4 sheet distorted into corrugated structure after the adsorption of Hg, compared with the initial configuration, which is in line with the previous results [45],[46]. Moreover, the change of the structure may have influence on the corresponding adsorption. Besides

Table 1

Adsorption energies (E_{ads}) and optimized structural parameters for Hg^0 adsorption on the different site of g-C_3N_4 model surface.

Site	E_{ads} (kJ mol^{-1})	d (Å)	R(Hg-C) (Å)	R(Hg-N) (Å)	Q_T (e)
H_{C1}	−114.8	2.748	4.043	3.676	0.02
H_{C2}	−154.4	2.840	3.738	3.506	0.01
H_{C3}	−153.4	2.880	3.679	3.596	0.01
H_{C4}	−154.4	2.835	3.745	3.508	0.01
H_1	−142.8	3.468	3.601	3.709	0.02
H_2	−161.1	3.498	3.542	3.689	0.02
H_3	−161.1	3.484	3.554	3.691	0.02
B_1	−162.2	3.423	3.473	3.616	0.02
B_2	−143.7	3.495	3.529	3.594	0.01

d is the height of the adsorbed Hg^0 measured from the surface; R(Hg-C) is the distance between the adsorbed Hg^0 and the nearest C atom; R(Hg-N) is distance between the adsorbed Hg^0 and the nearest N atom; Q_T denotes the total Mulliken charge on adsorbed Hg^0.

the adsorption energy, the distance of Hg atom to the neighbor C and N atoms was 3.473 Å and 3.616 Å, respectively. The C–Hg distance is much smaller than that of the bond length of Hg−Fe and Hg−Cl, which is respective 2.6 and 2.5 Å [47], and B-Hg of 2.09 Å [48]. The positive values (Q_T) of adsorbed Hg atom demonstrate that the adsorption was dominated by "donation" rather (electron transfer from Hg atom to g-C_3N_4) than "back donation" effects (charge transfer from g-C_3N_4 to Hg) [47],[49]. More importantly, Mulliken's charge analysis shows that the
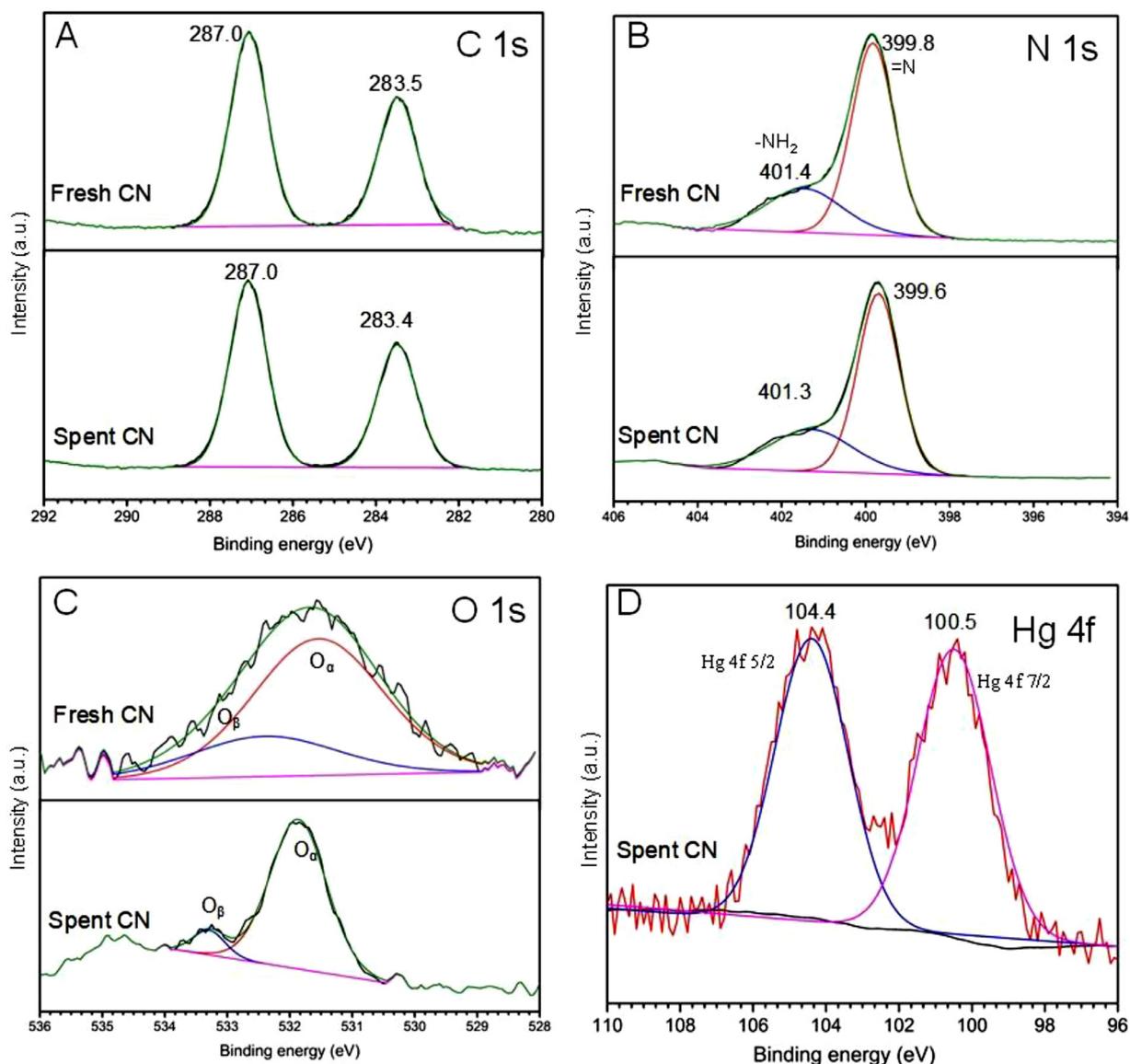
Fig. 4. XPS spectra of g-C$_3$N$_4$ before and after the adsorption. (A) C 1 s, (B) N 1 s, (C) O 1 s, and (D) Hg 4f.

electron transfer between Hg and C atoms near B$_1$ site of g-C$_3$N$_4$ was just 0.02 electron when the structure reached the stable state, which is much smaller than 0.120 reported by Ji et al. [32], 0.20 by Liu et al. [47], and 0.470 by Gao et al. [50]. According to the aforementioned analyses, we can conclude that the physisorption interaction exists between Hg atom and g-C$_3$N$_4$ without evident electron transfer.

3.4. Hg^0 adsorption and transformation mechanism

In order to examine whether Hg^0 is oxidized and what the species of adsorbed mercury on g-C$_3$N$_4$ surface is, the XPS tests were carried out and an insight on the XPS results is shown in Fig. 4. The C 1 s fitted into two principal peaks at the binding energies of ~287.0 eV and ~283.4 eV for the fresh and spent g-C$_3$N$_4$, respectively, indicating two different chemical environments of carbon existing in these two specimens [24]. The bands at ~287.0 eV relate to the reflection of $C - N - C$ coordination, while the bands at ~283.5 and ~283.4 eV are ascribed to the *sp^2* C atoms bonded to N in an aromatic ring [51]. For N 1 s peak, the bands at ~401.3 and ~401.4 eV are in accord with the amino functions. The bands at ~399.6 and ~399.8 eV correspond to the graphitic nitrogen [52]. The binding energies of C 1 s and N 1 s spectra of the

spent g-C$_3$N$_4$ show no evident values change compared with the fresh C$_3$N$_4$, indicating that the electron transfer effect between g-C$_3$N$_4$ and Hg° can be overlooked, i.e., the interaction between C$_3$N$_4$ and Hg^0 is physisorption. For O 1 s it can be deconvoluted into one dominating peak at binding energies of ~531.5 – 531.8 eV and ~532.4 – 533.3 eV for the fresh and spent C$_3$N$_4$, respectively. The phenomenon indicates two different chemical environments of oxygen existing in these two specimens as well. The bands at ~533.2 and ~533.3 eV correspond to oxygen (O$_\beta$) in adsorbed carbonates or water and hydroxyl groups, while the bands at ~531.5 and ~531.8 eV relate to the lattice oxygen (O$_\alpha$) [53]. The ratio of O$_\alpha$/O$_\beta$ was increased after the Hg^0 adsorption process, indicating that the lattice oxygen (O$_\alpha$) was increased during the Hg^0 removal process and involved in the mercury oxidation process derived from HgO [24], with a percentage of the chemisorbed oxygen increased from ~1.6 to ~5.3% for the g-C$_3$N$_4$ before and after the reaction, correspondingly, which infers a typical Mars-Maessen mechanism that the gaseous O$_2$ from the feed gas may replenish the depleted chemisorbed oxygen during the Hg^0 oxidation processes [24],[25],[54]. Besides, the characteristic peaks at 100.5 and 104.4 eV respectively corresponding to Hg 4f 7/2 and Hg 4f 5/2 that were assigned to HgO were found [24],[54]. The result indicated that the main species of mercury
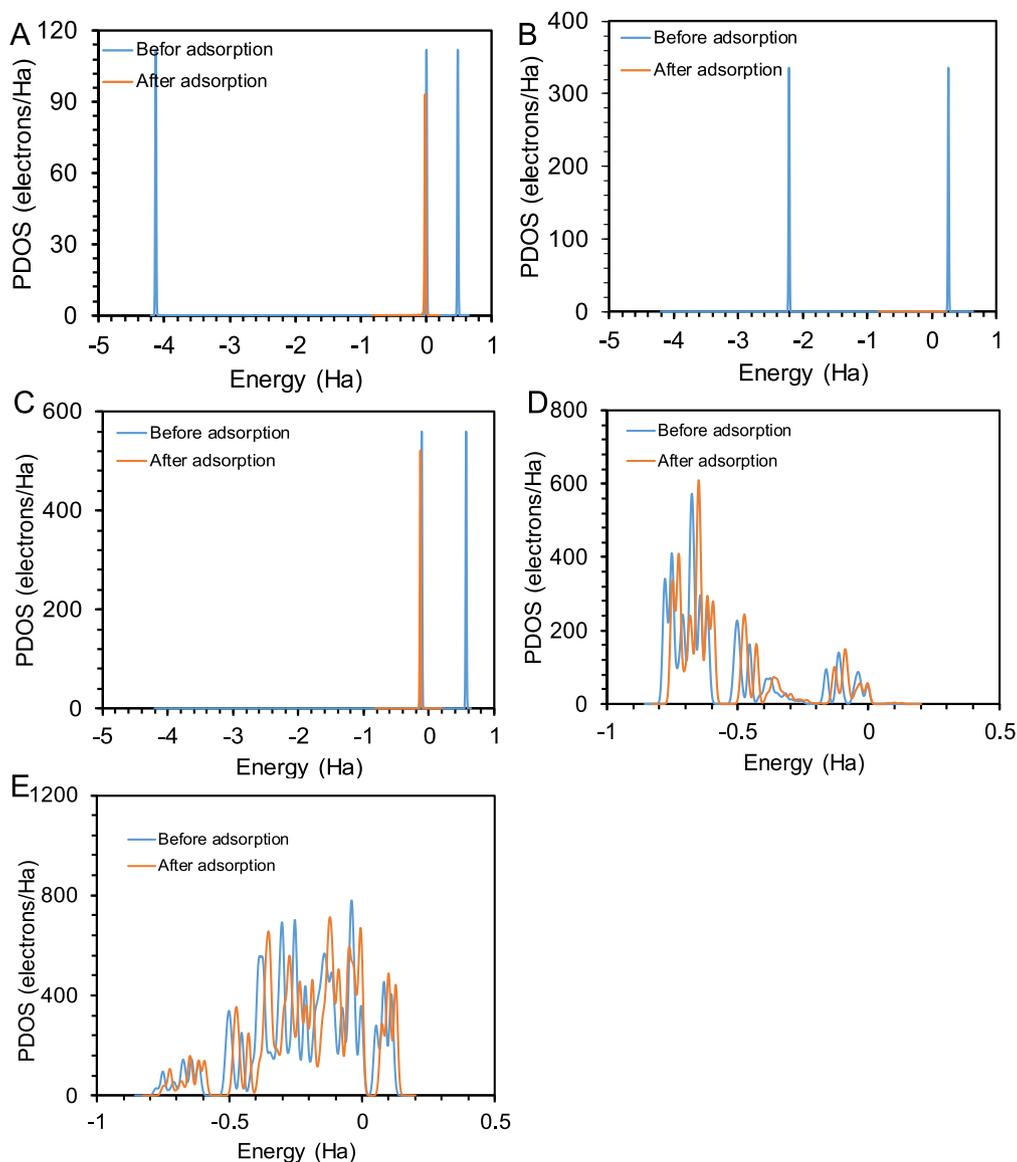
Fig. 5. PDOS of atoms (Hg, C_3N_4) for surface system before and after Hg^0 adsorption on g-C_3N_4 surface. (A) Hg s orbital; (B) Hg p orbital; (C) Hg d orbital; (D) s orbital of C and N; (E) p orbital of C and N. The Fermi level is set to be zero.

was HgO on the surface of 2D-g-C_3N_4 sample, and the electron transfer between g-C_3N_4 sorbent and Hg^0 was not evident, which well agrees with the results of DFT calculation. Thus, Hg^0 removal processes using 2D-g-C_3N_4 could be summarized into two stages: first the $Hg^0(g)$ and O_2 adhere on the 2D-g-C_3N_4 surface to form adhered mercury (Hg^0_{ads}) and chemisorbed oxygen (O_{ads}), and then the Hg^0_{ads} is oxidized into HgO by chemisorbed oxygen (O_{ads}). In addition, because HgO is stable only at temperature ~300 °C [55], the adsorbed HgO would decompose into elemental mercury again under the treatment of high temperature. Therefore, the used 2D-g-C_3N_4 can be relatively easily regenerated under thermal treatment.

3.5. Electronic structure

In general, density of states (DOS) indicates the number of states per energy interval at each level that can be occupied by electrons. To get an in-depth understanding of the Hg^0 adsorption mechanism on g-C_3N_4 surface, the partial density of states (PDOS) of Hg^0–2D-g-C_3N_4 was examined. The PDOS of the Hg atom adsorbed on the g-C_3N_4 surface are depicted in Fig. 5. As a comparison, the PDOS curve of isolated Hg atom

and pure g-C_3N_4 surface are also calculated. The Hg atom near B_1 site of g-C_3N_4 is shown by well-defined s- and d-orbitals near −0.03 and 0.60 Ha respectively, and an unfilled p-orbital near 0.25 Ha. After the adsorption process, all states of Hg atom shifted downward with the s- and p-orbital and decreased in energy for the Hg adsorbed configuration. In order to explore the binding mechanism of Hg atom on the g-C_3N_4 surfaces (B_1 site), the electrostatic potential was studied and shown in Fig. S4. The Hg atom was adsorbed on the B_1 site (i.e. the neighbor site of the yellow area, where was enriched with the electron), and the electron density change was relatively small before and after-adsorption process. This phenomenon was proved by the obtained value of Mulliken charge (Q_T), i.e., the electron transfer was not prominent with a physisorption mechanism.

As we know, C_3N_4 is a typical supramolecular semiconductor, which has an outstanding fluorescence effect associated with HOMO and LUMO [55–57]–[58]. In order to further clarify the electronic configuration of Hg^0-g-C_3N_4, the orbital calculation was implemented, as shown in Fig. 6. HOMO is mainly composed of the 2p orbital of low coordination N atoms in the surface, while LUMO is mainly composed of the 2p orbital of C atoms. The HOMO and LUMO position of g-C_3N_4 are
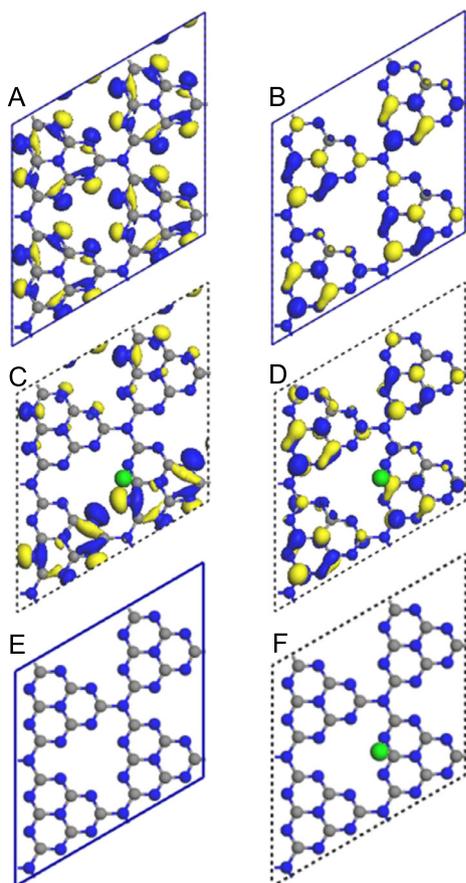
Fig. 6. HOMO (A) and LUMO (B) of g-C$_3$N$_4$; HOMO (C) and LUMO (D) of Hg^0-g-C$_3$N$_4$; The optimized geometry (E) and adsorbate configuration of g-C$_3$N$_4$ (F).

−5.14 eV and −3.86 eV (Vs. vacuum energy level), respectively, and the gap value is 1.34 eV. Whereas for the Hg^0-g-C$_3$N$_4$ system, the HOMO position is −6.19 eV, the LUMO position is −4.32 eV, and the gap is 1.87 eV. g-C$_3$N$_4$ is a typical supramolecular semiconductor which shows good photophysical properties with strong fluorescence and large Stokes shifts, and it can be used as optical chemical sensors [20],[42]. The Hg^0 adsorption has an obvious effect on the orbital structure of C$_3$N$_4$, and hence the optical property will change, and thus might be used as fluorescent chemical sensor for the Hg^0 detection.

4. Conclusion

A 2D-g-C$_3$N$_4$ nanosheet was prepared and employed as an adsorbent to adsorb element Hg^0, and exhibited a high Hg^0 removal efficiency (> 90%) at the condition of temperature 120 °C. The adsorption mechanism of Hg^0 on g-C$_3$N$_4$ surface was investigated thoroughly by XPS and density functional theory with the periodic cleavage 2D-g-C$_3$N$_4$ surface model. The experimental results and the followed calculations using density functional theory indicated the interaction between adsorbed elemental Hg^0 and 2D-g-C$_3$N$_4$ surface is physisorption interaction without prominent electron transfer, and the optimal adsorption site toward 2D-g-C$_3$N$_4$ is the bridge C–N site.

Declaration of Competing Interest

We declare that we have no financial and personal relationships with other people or organizations that can inappropriately influence our work, there is no professional or other personal interest of any nature or kind in any product, service and/or company that could be construed as influencing the position presented in, or the review of, the manuscript

entitled "DFT and Experimental Study of Elemental Mercury (Hg^0) Removal by 2D-g-C$_3$N$_4$".

Supplementary materials

Supplementary material associated with this article can be found, in the online version, at doi:10.1016/j.ceja.2021.100095.

References

[1] W. Xiang, J. Liu, M. Chang, C. Zheng, The adsorption mechanism of elemental mercury on CuO (110) surface, Chem. Eng. J. 200 (2012) 91–96.

[2] R. Ochoa-Gonzalez, P. Cordoba, M. Diaz-Somoano, O. Font, M.A. Lopez-Anton, C. Leiva, M.R. Martinez-Tarazona, X. Querol, C.F. Pereira, A. Tomas, P. Gomez, P. Mesado, Differential partitioning and speciation of Hg in wet FGD facilities of two Spanish PCC power plants, Chemosphere 85 (2011) 565–570.

[3] S. Wang, L. Zhang, L. Wang, Q. Wu, F. Wang, J. Hao, A review of atmospheric mercury emissions, pollution and control in China, Front. Environ. Sci. Eng. 8 (2014) 631–649.

[4] X. Fu, X. Feng, J. Sommar, S. Wang, A review of studies on atmospheric mercury in China, Sci. Total Environ. 421 (2012) 73–81.

[5] R.A. Monterrozo, M. Fan, M.D. Argyle, Adsorption of mercury with modified thief carbons, J. Environ. Eng. 138 (2012) 386–391.

[6] C.M. Bergeron, C.M. Bodinof, J.M. Unrine, W.A. Hopkins, Mercury accumulation along a contamination gradient and nondestructive indices of bioaccumulation in amphibians, Environ. Toxicol. Chem. 29 (2010) 980–988.

[7] A. Fuente-Cuesta, M.A. Lopez-Anton, M. Diaz-Somoano, M.R. Martínez-Tarazona, Retention of mercury by low-cost sorbents: influence of flue gas composition and fly ash occurrence, Chem. Eng. J. 213 (2012) 16–21.

[8] V. Basavarao, Adsorption studies on treatment of textile dyeing industrial effluent by fly ash, Chem. Eng. J. 116 (2006) 77–84.

[9] Q. Zhang, Q. Yang, P. Phanlavong, Y. Li, Z. Wang, T. Jiao, Q. Peng, Highly efficient lead(II) sequestration using size-controllable polydopamine microspheres with superior application capability and rapid capture, ACS Sustain. Chem. Eng. 5 (2017) 4161–4170.

[10] B. Wang, J. Xia, L. Mei, L. Wang, Q. Zhang, Highly efficient and rapid lead(II) scavenging by the natural artemia cyst shell with unique three-dimensional porous structure and strong sorption affinity, ACS Sustain. Chem. Eng. 6 (2018) 1343–1351.

[11] Y.H. Li, C.W. Lee, B.K. Gullett, Importance of activated carbon's oxygen surface functional groups on elemental mercury adsorption, Fuel 82 (4) (2003) 451–457.

[12] S. Yang, Y. Guo, N. Yan, Z. Qu, J. Xie, C. Yang, J. Jia, Capture of gaseous elemental mercury from flue gas using a magnetic and sulfur poisoning resistant sorbent Mn/gamma-Fe$_2$O$_3$ at lower temperatures, J. Hazard. Mater. 186 (2011) 508–515.

[13] H. Li, C.Y. Wu, Y. Li, J. Zhang, Superior activity of MnOx-CeO$_2$/TiO$_2$ catalyst for catalytic oxidation of elemental mercury at low flue gas temperatures, Appl. Catal., B 111 (2012) 381–388.

[14] J. Xie, N. Yan, S. Yang, Z. Qu, W. Chen, W. Zhang, K. Li, P. Liu, J. Jia, Synthesis and characterization of nano-sized Mn-TiO$_2$ catalysts and their application to removal of gaseous elemental mercury, Res. Chem. Intermed. 38 (9) (2012) 2511–2522.

[15] Z. Mei, Z. Shen, W. Wang, Y. Zhang, Novel sorbents of non-metal-doped spinel Co$_3$O$_4$ for the removal of gas-phase elemental mercury, Environ. Sci. Technol. 42 (2008) 590–595.

[16] X. Gao, Y. Zhou, Y. Tan, Z. Cheng, B. Yang, Ma Y., Z. Shen, J. Jia, Exploring adsorption behavior and oxidation mechanism of mercury on monolayer Ti$_2$CO$_2$ (MXenes) from first principles, Appl. Surf. Sci. 464 (2019) 53–60 2019.

[17] X. Gao, Y. Zhou, S. Liu, Y. Tan, Z. Cheng, Z. Shen, FeN$_3$-embedded carbon as an efficient sorbent for mercury adsorption: a theoretical study, Chem. Eng. J. 374 (2019) 1337–1343.

[18] Y. Lu, B. Jiang, L. Fang, F.L. Ling, J.M. Gao, F. Wu, X.H. Zhang, High performance NiFe layered double hydroxide for methyl orange dye and Cr(VI) adsorption, Chemosphere 152 (2016) 415–422.

[19] T. Yan, T. Chen, X. Wang, F. Jiang, Adsorption of perfluorooctane sulfonate (PFOS) on mesoporous carbon nitride, RSC Adv. 3 (2013) 22480–22489.

[20] Y. Li, J. Zhang, Q. Wang, Y. Jin, D. Huang, Q. Cui, G. Zou, Nitrogen-rich carbon nitride hollow vessels: synthesis, characterization, and their properties, J. Phys. Chem. B 114 (2010) 9429–9434.

[21] Y. Yu, J. Geng, H. Li, R. Bao, H. Chen, W. Wang, J. Xia, W.Y. Wong, Exceedingly high photocatalytic activity of g-C$_3$N$_4$/Gd-N-TiO$_2$ composite with nanoscale heterojunctions, Sol. Energ. Mat. Sol. C. 168 (2017) 91–99.

[22] M. Karimi-Nazarabad, E.K. Goharshadi, Highly efficient photocatalytic and photoelectrocatalytic activity of solar light driven WO$_3$/g-C$_3$N$_4$ nanocomposite, Sol. Energ. Mat. Sol. C. 160 (2017) 484–493.

[23] Y. Li, Y. Xue, J. Tian, X. Song, X. Zhang, X. Wang, H. Cui, Silver oxide decorated graphitic carbon nitride for the realization of photocatalytic degradation over the

full solar spectrum: from UV to NIR region, Sol. Energ. Mat. Sol. C. 168 (2017) 100–111.

[24] D. Liu, Z. Zhang, J. Wu, Elemental mercury removal by MnO_2 nanoparticle-decorated carbon nitride nanosheet, Energ. Fuel. 33 (2019) 3089–3097.

[25] Z. Zhang, J. Wu, D. Liu, Co_3O_4/g-C_3N_4 Hybrids for gas-phase Hg^0 removal at low temperature, Processes 7 (2019) 279–290.

[26] X. Zhang, D. Wang, X. Man, J. Wu, Q. Liu, Y. Qi, Z. Liu, X. Zhao, J. Wu, C. Hao, Simultaneous catalytic oxidation of nitric oxide and elemental mercury by single-atom Pd/g-C_3N_4 catalyst: a DFT study, J. Colloid Interf. Sci. 558 (2020) 123–136.

[27] X. Liu, Z. Gao, H. Huang, G. Yan, T. Huang, C. Chen, W. Yang, X. Ding, Influence of BiOIO3 morphology on the photocatalytic efficiency of Z-scheme $BiOIO_3$/g-C_3N_4 heterojunctioned composite for Hg^0 removal, Mol. Catal. 488 (2020) 110901.

[28] Q. Li, L. Xu, K.W. Luo, W.Q. Huang, L.L. Wang, X.F. Li, G.F. Huang, Y.B. Yu, Insights into enhanced visible-light photocatalytic activity of C_{60} modified g-C_3N_4 hybrids: the role of nitrogen, Phys. Chem. Chem. Phys. 18 (2016) 33094–33102.

[29] T. Yan, H. Chen, F. Jiang, X. Wang, Adsorption of perfluorooctane sulfonate and perfluorooctanoic acid on magnetic mesoporous carbon nitride, J Chem. Eng. Data 59 (2014) 508–515.

[30] C. Shen, C. Chen, T. Wen, Z. Zhao, X. Wang, A. Xu, Superior adsorption capacity of g-C_3N_4 for heavy metal ions from aqueous solutions, J. Colloid Interf. Sci. 456 (2015) 7–14.

[31] Liu S, L. Chen, X. Mu, M. Xu, J. Yu, G. Yang, X.Luo G., H. Zhao, T. Wu, Development of Pd_n/g-C_3N_4 adsorbent for Hg^0 removal–DFT study of influences of the support and Pd cluster size, Fuel 254 (2019) 115537.

[32] W. Ji, Z. Shen, M. Fan, P. Su, Q. Tang, C. Zou, Adsorption mechanism of elemental mercury (Hg^0) on the surface of $MnCl_2$ (110) studied by density functional theory, Chem. Eng. J. 283 (2016) 58–64.

[33] B. Delley, Ground-state enthalpies: evaluation of electronic structure approaches with emphasis on the density functional method, J. Phys. Chem. A 110 (2006) 13632–13639.

[34] G. Liu, S. You, Y. Tan, N. Ren, In situ photochemical activation of sulfate for enhanced degradation of organic pollutants in water, Environ. Sci. Technol. 51 (2017) 2339–2346.

[35] B. Delley, From molecules to solids with the $Dmol^3$ approach, J. Chem. Phys. 113 (2000) 7756–7764.

[36] Y. Deng, L. Tang, G. Zeng, Z. Zhu, M. Yan, Y. Zhou, J. Wang, Y. Liu, J. Wang, Insight into highly efficient simultaneous photocatalytic removal of Cr (VI) and 2,4-diclorophenol under visible light irradiation by phosphorus doped porous ultrathin g-C_3N_4 nanosheets from aqueous media: performance and reaction mechanism, Appl. Catal. B-Environ. 203 (2017) 343–354.

[37] X. Hu, H. Ji, F. Chang, Y. Luo, Simultaneous photocatalytic Cr (VI) reduction and 2,4,6-TCP oxidation over g-C_3N_4 under visible light irradiation, Catal. Today 224 (2014) 34–40.

[38] X. Wang, K. Maeda, A. Thomas, K. Takanabe, G. Xin, J.M. Carlsson, K. Domen, M. Antonietti, A metal-free polymeric photocatalyst for hydrogen production from water under visible light, Nat. Mater. 8 (2009) 76–80.

[39] L. Ge, Synthesis and photocatalytic performance of novel metal-free g-C_3N_4 photocatalysts, Mater. Lett. 65 (2011) 2652–2654.

[40] A.I. Finkel, N.V. Spiridonova, Chemical properties and molecular structure of derivatives of sym-heptazine [1,3,4,6,7,9,9b-heptaazaphenalene, tri-1,3,5-triazine], Russ. Chem. Rev. 33 (1964) 399–405.

[41] M.J. Bojdys, J.O. Muller, M. Antonietti, A. Thomas, Ionothermal synthesis of crystalline, condensed, graphitic carbon nitride, Chem. Eur. J. 14 (2008) 8177–8182.

[42] B.V. Lotsch, M. Döblinger, J. Sehnert, L. Seyfarth, J. Senker, O. Oeckler, W. Schnick, Unmasking melon by a complementary approach employing electron diffraction, solid-state NMR spectroscopy, and theoretical calculations-structural characterization of a carbon nitride polymer, Chem. Eur. J. 13 (2007) 4969–4980.

[43] Q. Xiang, J. Yu, M. Jaroniec, Preparation and enhanced visible-light photocatalytic H_2-production activity of graphene/C_3N_4 composites, J. Phys. Chem. C115 (2011) 7355–7363.

[44] S.L. Li, H. Yin, X. Kan, L.Y. Gan, U. Schwingenschlögl, Y. Zhao, Potential of transition metal atoms embedded in buckled monolayer g-C_3N_4 as single-atom catalysts, Phys. Chem. Chem. Phys. 19 (2017) 30069–30077.

[45] D. Ghosh, G. Periyasamy, B. Pandey, S.K. Pati, Computational studies on magnetism and the optical properties of transition metal embedded graphitic carbon nitride sheets, J. Mater. Chem. C 2 (2014) 7943–7951.

[46] X. Ma, X. Li, M. Li, X. Ma, L. Yu, Y. Dai, Effect of the structure distortion on the high photocatalytic performance of C_{60}/g-C_3N_4 composite, Appl. Surf. Sci. 414 (2017) 124–130.

[47] T. Liu, L. Xue, X. Guo, Y. Huang, C. Zheng, DFT and experimental study on the mechanism of elemental mercury capture in the presence of HCl on α-Fe_2O_3 (001), Environ. Sci. Technol. 50 (2016) 4863–4868.

[48] X. Gao, Y. Zhou, Y. Tan, Z. Cheng, Q. Tang, J. Jia, Z. Shen, Unveiling adsorption mechanisms of elemental mercury on defective boron nitride monolayer: a computational study, Energ. Fuel. 32 (2018) 5331–5337.

[49] Y. Zhou, W. Chu, F. Jing, J. Zheng, W. Sun, Y. Xue, Enhanced hydrogen storage on Li-doped defective graphene with b substitution: a DFT study, Appl. Surf. Sci. 410 (2017) 166–176.

[50] A. Vinu, Two-dimensional hexagonally-ordered mesoporous carbon nitrides with tunable pore diameter, surface area and nitrogen content, Adv. Funct. Mater. 18 (2008) 816–827.

[51] Z. Teng, H. Lv, C. Wang, H. Xue, H. Pang, G. Wang, Bandgap engineering of ultrathin graphene-like carbon nitride nanosheets with controllable oxygenous functionalization, Carbon N Y 113 (2017) 63–75.

[52] L.J. France, Q. Yang, W. Li, Z. Chen, J. Guang, D. Guo, L. Wang, X. Li, Ceria modified FeMnOx—Enhanced performance and sulphur resistance for low-temperature SCR of NOx, Appl. Catal. B-Environ. 206 (2017) 203–215.

[53] H. Xu, Z. Qu, C. Zong, W. Huang, F. Quan, N. Yan, MnO_x/graphene for the catalytic oxidation and adsorption of elemental mercury, Environ. Sci. Technol. 49 (2015) 6823–6830.

[54] S. Yang, Y. Guo, N. Yan, D. Wu, H. He, Z. Qu, J. Jia, Elemental mercury capture from flue gas by magnetic Mn–Fe spinel: effect of chemical heterogeneity, Ind. Eng. Chem. Res. 50 (2011) 9650–9656.

[55] J. Fu, J. Yu, C. Jiang, B. Cheng, g-C_3N_4-based heterostructured photocatalysts, Adv. Energy Mater. (2017) 1701503–1701534.

[56] L.Y. Chen, W.D. Zhang, In_2O_3/g-C_3N_4 composite photocatalysts with enhanced visible light driven activity, Appl. Surf. Sci. 301 (2014) 428–435.

[57] Y. Sun, W. Zhang, T. Xiong, Z. Zhao, F. Dong, R. Wang, W.K. Ho, Growth of BiOBr nanosheets on C_3N_4 nanosheets to construct two-dimensional nanojunctions with enhanced photoreactivity for NO removal, J. Colloid Interface Sci. 418 (2014) 317–323.

[58] G. Liu, S. You, Y. Zhang, H. Huang, H. Spanjers, Conjugated donor-acceptor (DA) supramolecule catalyst for visible-light-driven photocatalytic removal of bromate in water, J. Colloid Interf. Sci. 553 (2019) 666–673.